Main text

Cracking resistance of nanostructured freestanding tungsten films

S.E. Naceri[*1], M. Rusinowicz[2], M. Coulombier[1], T. Pardoen[*1,3]

[1] Institute of Mechanics, Materials and Civil Engineering (IMMC), UCLouvain, 1348 Ottignies-Louvain-la-Neuve, Belgium

[2] Mines Saint-Etienne, CNRS, UMR5307 LGF, Centre SMS, 42023 Saint Etienne, France

[3] WEL Research Institute, avenue Pasteur, 6, 1300 Wavre, Belgium

Corresponding authors: S.E. Naceri (salaheddine.naceri@uclouvain.be), T. Pardoen (thomas.pardoen@uclouvain.be)

Keywords: Fracture toughness, miniaturised mechanical testing, tungsten films, residual stresses, nuclear fusion.

Abstract

The fracture toughness K_c of freestanding tungsten films is explored using a MEMS-based crack-on-chip method and multiscale finite element modelling, in the context of miniaturised testing of structural materials for nuclear fusion applications. The primary ambition is to determine to what extent testing thin nanostructured tungsten films can provide relevant data with respect to bulk tungsten fracture behavior, particularly in view of irradiation testing. The second objective is to enhance fundamental knowledge on the cracking behavior of thin metallic films with a quasi-brittle response. Tungsten films with 370 nm thickness are deposited by magnetron sputtering under different pressures and characterized using grazing incidence X-ray diffraction, surface curvature measurements, scanning electron microscopy and nano-indentation. Microstructure evolution, residual stresses, and tensile properties are analyzed to confirm the BCC α-phase. The fracture toughness of the tungsten films is determined on-chip using a crack arrest approach and finite element modelling to extract K_{Ic}. The analysis conducted on 90 successful test structures provides an average fracture toughness value of 3.2 ± 0.36 MPa √m. This value is typically, 50% lower than for bulk tungsten, despite the

submicron thickness, while the same intergranular fracture mechanism is observed. The link with crack tip plasticity is further unravelled by extended finite element simulations relying on a cohesive zone model. Care is taken to properly resolve the mechanical behavior of the nanometer scale fracture process zone. The calibrated peak strength is equal 7.8 GPa, which is less than two times the large yield stress of the nanocrystalline film. With such a ratio, the impact of plasticity outside the fracture process zone is limited, corresponding to negligible R curve effect and extra dissipation upon crack growth in contrast with bulk specimens for which a ratio above four is expected.

1. Introduction

Tungsten (W) is considered the primary choice for plasma-facing parts in both the International Thermonuclear Experimental Reactor (ITER) and the DEMOnstrator power plant (DEMO), two devices designed to demonstrate the feasibility of nuclear fusion technology **[1-3]**. Its suitability for the divertor armor and as a part of the breeding blanket comes from the unique combination of high melting point (≈ 3422 °C), excellent thermal conductivity, low irradiation-induced swelling, minimal sputtering yield, and low tritium retention **[4-6]**. However, tungsten also has limitations as well, notably a relatively high ductile-to-brittle transition temperature (DBTT) between 200 and 600 °C, which is influenced by several factors **[7]** including working **[8-10]**, grains orientation **[11]**, and the presence of impurities **[12]**, making it brittle at low temperatures. Other drawbacks include embrittlement due to low recrystallisation temperature, as well as neutron- and helium-induced embrittlement **[13,14].**

Previous studies primarily investigated the behavior of bulk W at elevated temperatures under high heat flux conditions using electron beam heating and numerical simulations **[15-22]**. Cracks formed in W under these conditions extend from the surface to depths of micrometres to millimeters. At lower temperatures, below DBTT, efforts to improve thermo-mechanical

performance have been based on microstructural refinement, mechanical treatments, alloying, and particle reinforcement **[23-27]**. Even in the steady state regime with heat fluxes of 5-10 MW/m², W will experience severe cyclic thermal loads in the daily operation of the future DEMO reactor **[28,29]**. These cyclic loads induce significant stresses during the heating and cooling phases, leading to potential crack propagation when the stress intensity factor exceeds the fracture toughness K_{Ic} of tungsten. Hence, knowledge of fracture toughness and its variation with microstructure, temperature, strain rate, and crack orientation is critical for predicting material durability **[14,29-33]**.

The fracture toughness of bulk W has been extensively studied through macroscopic experiments. Typically, room temperature K_{Ic} ranges between 6 and 12 MPa√m with variations depending on whether it is polycrystalline rolled, sintered or single-crystal bulk tungsten **[30-33]**. At small scales, several studies relied on notched microcantilevers to investigate the fracture behavior of W. For instance, Wurster et al. **[34]** developed a procedure based on elastic-plastic fracture mechanics (EPFM) with the J-integral and Crack-Tip Opening Displacement (CTOD) parameters to extract the fracture toughness of single-crystal tungsten microcantilevers. Stable crack propagation was found in contrast to the unstable cracking in macroscale specimens. Similarly, Ast et al. **[35]** demonstrated a dependence of K_{Ic} on specimen size, with smaller cantilevers exhibiting lower toughness than larger ones. However, once a critical size was reached, the fracture toughness plateaued to values between 5.5 and 6.5 MPa√m. Extending this size-dependent behavior to W composite systems, Schmuck et al. **[36]** observed a size effect in W–Cu nanocomposites, with fracture toughness increasing from 5.5 to 6.2 MPa√m as cantilever size grew from 5 × 5 to 35 × 35 μm². Shifting focus from size effects to grain boundary properties, Tian et al. **[37]** reported grain boundary embrittlement in recrystallised W, with toughness dropping to 4.7 MPa√m, compared to 14.5 MPa√m for single

grains and 19 MPa√m for as-received material processed by sintering and two-directional forging.

These studies illustrate that the fracture toughness of micro-sized tungsten samples can differ significantly from bulk, but without a definitive conclusion on whether the variations depend on specimen size as a result of constraint effect, on experimental bias due for instance to the pre-cracking method, on changes in failure modes and/or on differences in the microstructure and segregation of impurities at grain boundaries.

One of the main concerns with microscale testing, particularly using the Focused Ion Beam (FIB) technique for specimen preparation, is the adverse effect of ion implantation that can alter material properties near the notch or the pre-crack tip. This has raised questions about the reliability of fracture toughness measurements on FIB-prepared specimens **[38]**. As a result, alternative approaches that minimize these effects are being explored to ensure robust results **[39-42]**. Furthermore, the nature of the failure mechanisms in the submicron films must be determined, as well as the development of crack tip plasticity and potential impact on dissipation and size dependency, to make a link with the results on bulk specimens. Finally, a remnant difficulty lies in the preparation of test specimens with sufficiently sharp pre-cracks, with an opening ideally smaller than the critical CTOD; otherwise, the starter crack is not a real crack but a notch. If this condition is not fulfilled, extra dissipation is needed to initiate the crack **[43]**

In the context of the growing need to miniaturize test methods, particularly to address challenges in scaling down towards coating-type applications and to reduce cost, time, space, and radioactive waste compared to bulk material irradiation testing, this study aims at determining the fracture toughness of nanostructured freestanding W films, at exploring the representativeness with bulk W toughness, at investigating the cracking mechanism, and at assessing the feasibility of advancing towards irradiation testing. We employ a

MicroElectroMechanical-based testing approach nicknamed Crack-On-Chip (COC), which has been developed and refined over the years at UCLouvain as an extension of the original lab-on-chip method **[39,44]** and has demonstrated reliable results across various materials (Al_2O_3, SiO_2, Si_3N_4, Cu, etc.) **[40–42]**. Here, we showcase the feasibility of on-chip fracture mechanics testing for tungsten and adapt the data reduction scheme. As the test is based on a crack arrest method, it means that the determined fracture toughness is not the initiation toughness due to possible R-curve effect during crack propagation. For this reason, finite element simulations relying on the XFEM method with a description of the fracture process through a cohesive zone model are performed to separate the energy spent in the fracture process zone and the extra plastic dissipation around the crack tip and crack wake. This is a challenging task in view of the very small extent of the fracture process zone that requires extremely fine discretization. Once calibrated, the CZM traction separation law provides the relevant information on the failure process. Such a model, in addition to providing a foundation to understand the experiments, offers a path towards transferring data obtained on microscopic test specimens to bulk specimens and macroscopic components as used in fusion reactors.

2. Materials and methods

2.1. Processing of tungsten thin films

Tungsten films were deposited by DC magnetron sputtering in a VST-TFDS 462 system on a (100) oriented Si substrate using a 99.99 % pure W target. The pressure in the deposition chamber was initially reduced to approximately 4.5×10^{-7} Torr, followed by the introduction of high-purity argon (99.9999 %) as the working gas prior to deposition. During deposition, the substrate-target distance was set to 50 mm, with the substrate holder positioned at an angle relative to the sputtering target and rotated at a speed of 8 rpm. The deposition power was kept constant at 250 watts, and the argon pressure and target cleaning time were adjusted to fine-tune the deposition conditions. After deposition, the W films were annealed to reduce residual

stresses which are detrimental to proper deployment of the chip test method. This was accomplished in a vacuum tube with a 200 sccm argon flow to minimize contamination or oxidation of the tungsten layers. The process consisted of gradually heating the films from room temperature to 600 °C, holding them at this temperature for two hours, followed by slow cooling through natural furnace cooling. The film thickness for nanoindentation testing was set to 1000 nm to limit substrate effects, while the film used in the crack-on-chip method was 370 nm thick.

2.2. Microstructural characterization and residual stress measurements

Grazing Incidence X-Ray Diffraction (GIXRD) with a copper tube X-ray source (CuKα = 1.540598 Å) was used to identify the crystallographic phase. This technique, which provides enhanced surface sensitivity, was used to minimize substrate interference by applying a grazing angle of incidence of about 0.6 °, thereby ensuring a stronger signal from the film. The surface and grain morphology were characterized using a Zeiss Scanning Electron Microscope (SEM). In addition, surface curvature measurements were systematically performed to evaluate the residual stresses using a Veeco Dektak 150 profilometer and applying the Stoney equation **[45]**, as follows:

$$\sigma_{film} = \frac{1}{6}\frac{E_s}{1-\nu_s}\frac{t_s^2}{t_f}\left(\frac{1}{R_{AD}} - \frac{1}{R_{BD}}\right) \quad (1)$$

where $\boldsymbol{R_{AD}}$ and $\boldsymbol{R_{BD}}$ are the radius of curvature after and before film deposition, respectively, $\boldsymbol{t_f}$ and $\boldsymbol{t_s}$ are the film and substrate thickness, respectively, and $\boldsymbol{E_s/(1-\nu_s)}$ is the biaxial elastic modulus of the silicon substrate.

2.3. Instrumented nanoindentation tests

The elastic-plastic properties of the films were determined through instrumented nanoindentation with the DCM load-controlled head from the Agilent G200 system. A diamond Berkovich tip was used whose area function, relating the projected contact area A_c to the contact

depth h_c, was derived from a fused silica reference sample according to the Oliver and Pharr procedure **[46]**. The tests were performed with a target constant strain rate of 0.05 s^{-1} up to a maximum depth of 400 nm, using the Continuous Stiffness Measurement (CSM) mode to monitor the evolution of the contact stiffness *S*. The apparent elastic modulus *E* and hardness *H* were estimated using Sneddon's equation **[47,48]** and Meyer's definition **[49]**, respectively:

$$E^* = \frac{\sqrt{\pi}}{2}\frac{S}{\sqrt{A_c}} \quad , \quad \frac{1}{E^*} = \frac{1-\nu_t^2}{E_t} + \frac{1-\nu^2}{E}, \tag{2}$$

$$H = \frac{F}{A_c} \tag{3}$$

where E^* is the reduced elastic modulus, E_t = 1141 GPa and ν_t = 0.07 are the elastic modulus and Poisson ratio of the diamond tip, ν is the Poisson ratio of tungsten set to 0.28, and F is the applied load. The projected contact area A_c was estimated using the Oliver and Pharr model **[46]**. The film's modulus E_f was derived using the Hay and Crawford model based on the apparent modulus E **[50]**. Finally, from the hardness H, the representative stress σ_r corresponding to the flow stress associated with ~ 8 % plastic strain was estimated using Kermouche's model **[51]**.

2.4. Crack-on-chip experimental method

The COC method **[40-42]** is based on the deformation of a notched freestanding thin film specimen, which is produced by releasing the high internal stresses of an actuator beam structure to which the test specimen is attached. This causes a crack to initiate and propagate from the notch tip until it arrests when the energy release rate drops to its critical value. The fracture toughness of the film is determined by measuring the crack length after the test and by using a finite element (FE) model described later to extract the *K* value. The crack arrest nature of the test solves the difficulty of preparing a perfectly sharp initial pre-crack, assuming that the crack has propagated long enough to avoid any influence from the starter notch.

The design of this novel technique begins with the deposition of a 1 μm thick sacrificial layer of silicon dioxide (SiO_2) on a silicon (Si) substrate using Plasma Enhanced Chemical Vapor Deposition (PECVD). Next, a 200 nm thick layer of silicon nitride SiN (Si_3N_4) is deposited on top of the SiO_2 layer by Low-Pressure Chemical Vapor Deposition (LPCVD) and patterned using photolithography/etching into the shape of an actuator consisting of two long beams. This SiN layer was selected because of its large tensile internal stress of about 1 GPa and its isotropic linear elastic behavior. Finally, in the last step, the 370 nm thick W sample layer is deposited on top of the stack and patterned, forming a notched double cantilever-type beam that is attached to the two horizontal actuator beams. This planar fabrication process allows a large number of test structures to be produced and hundreds of specimens to be tested on a single chip.

The mechanical test is initiated by releasing the internal stress in the SiN actuator through chemically etching the SiO_2 sacrificial layer with a hydrofluoric acid solution. The two SiN beams pull on the notched W-free beam, initiating and propagating a crack until it arrests in the structure. An SEM micrograph of a COC test structure after the release of internal stress in the SiN actuator is provided in **Fig.1a**, with a zoomed-in view of the arrested crack in the W specimen, shown in **Fig.1b**. The Si die containing the COC test structures is then examined in a SEM to measure the relevant geometrical parameters, particularly the crack arrest length, as an input for the finite element simulation of the test presented in **Section 2.5**. Further details on the COC method, including fabrication steps and test execution, can be found in the Supplementary Materials, **section A**.

2.5. Crack-on-chip numerical modelling

Finite element simulations were conducted using the commercial software ABAQUS® to develop an accurate data reduction scheme for extracting the stress intensity factor K and from there the critical stress intensity factor K_{Ic}. Three different models were used, all relying on a

large strain setting. These models consisted of two deformable bodies represented within a single domain divided into partitions, including the W specimen and the SiN actuator as well as the surrounding area around the test structure. The elastic behavior of these materials was assumed to be linear isotropic. The elastic moduli were measured by nanoindentation and found to be equal to 360 GPa for W and 250 GPa for SiN (with Poisson ratios fixed at 0.28 and 0.3, respectively). The J_2 flow theory was chosen to represent the plastic yielding in the W specimen with a Swift isotropic hardening law: ($\sigma_0 = k\,\varepsilon^n$), where σ_0 is the yield strength of W, k is the hardening coefficient taken here equal to σ_0/E and n is the strain hardening exponent. The residual stresses measured experimentally in the two materials were introduced in the FE models as predefined fields, being - 0.7 GPa for W and + 1 GPa for SiN.

Each simulation consists of two steps representing the state of the crack-on-chip test structure before and after release. In the first step, the entire structure is fully constrained, while, in the second step, these boundary conditions are progressively removed from the W specimen, the two actuator beams, and the over-etched length surrounding the test structure. The ABAQUS®/Standard solver was used.

The first FE model is a 2D plane stress model with a static crack and a purely isotropic linear elastic description, where the energy release rate is calculated using the J-integral method. The crack is modelled by creating a partition as a 1D straight line starting at the notch tip and extending along the specimen length. This line represents the crack generated in the actual test, and its length is adjusted based on experimental measurement of the crack extension Δa. A seam crack is defined along this line using the options available in ABAQUS. Several contours are used to estimate the J integral and verify the path independency. The J integral is then converted into a stress intensity factor K_I using the relationship $K_I = \sqrt{E\,J}$ under plane stress conditions (see **Fig. 4c**). The choice of plane stress versus plane strain condition will be justified

a posteriori based on plastic zone size (and will turn to be unimportant in the case of a purely linear elastic model).

The second model is a 2D plane strain elastic-plastic model, where crack propagation was simulated using the extended Finite Element Method (XFEM) and a traction-separation law. A starter crack of 50 nm was introduced into the tungsten film at the notch tip to help triggering crack initiation. The XFEM method was used to simulate the propagation of this starter crack during the release of the SiN actuator residual stresses without remeshing. XFEM was particularly well suited due to the extreme degree of mesh refinement needed for these simulations as shown later in the results section, the fracture process zone (FPZ) size will extend over only a few nanometers, which must be sufficiently discretized.

A bilinear traction-separation law, involving two main material properties being the peak stress $\hat{\sigma}$ and critical opening δ_c, was chosen to describe the local failure mechanisms in the fracture process zone. Cracking initiates when the maximum principal tensile stress exceeds the peak stress $\hat{\sigma}$. When this stress is reached locally, the traction decreases linearly until it vanishes at a critical opening δ_c, corresponding to the distance beyond which there is no longer any load carrying capacity. Crack propagation is thus dictated by the fracture energy $\Gamma_0 = \frac{1}{2}\hat{\sigma}\delta_c$, which, in the case of purely brittle behavior, corresponds to the critical energy release rate at initiation J_c. In this work, we have chosen to adjust the parameters ($\hat{\sigma}$, Γ_0), while δ_c is directly derived from this pair of values.

The third model is a 3D static elastic model constructed to verify the hypotheses of the 2D models and, ultimately, their validity for instance regarding the impact of a plane stress versus plane strain setting or the presence of small bending effects. The in-plane geometry was reproduced identically to the 2D models but with thicknesses equal to 190 nm for the SiN actuator and 370 nm for the W specimen, which, being thicker, has its upper part higher than

that of the actuator. An example of a finite element model (3D J-integral) of the crack-on-chip test is provided in **Fig. 1c**, with a zoomed-in view of the crack extension Δa as measured experimentally in **Fig. 1d.**

3. Experimental results

3.1. Microstructure and residual stress of tungsten films

When deposited as a film, tungsten can exhibit two distinct crystal phases: the α-phase, which has a body-centered cubic (BCC) structure similar to bulk W but with a much smaller grain size, and the β-phase, which has an A15 structure. The choice of deposition parameters, particularly the working gas pressure, is critical in determining the resulting phase **[52-54]**, as well as the residual stresses. Ten different DC magnetron sputtering deposition conditions were tested by varying the argon partial pressure over a wide range from 1 to 15 mTorr. **Fig. 2a** shows the variation of the residual stress as determined from the Stoney equation under these different conditions. Note that more details on phase identification by GIXRD and microstructure analysis by SEM are provided as Supplementary Materials (**section B**). Argon pressures between 1 and 8 mTorr led to the formation of the α-phase with compressive residual stresses ranging from - 2.5 to - 1 GPa, while argon pressures between 9 and 15 mTorr induced the formation of the β-phase with tensile residual stresses ranging from + 1 to + 2 GPa. In order to align with the structure of bulk W, we selected the α-phase while minimizing residual stresses to avoid out-of-plane deformation problems during COC tests (**section B**). Thus, an argon pressure of 6 mTorr was selected, resulting in the formation of the α-phase with residual stress at around - 1.2 GPa. Subsequent annealing at 600 °C for 2 h further reduced the stress level, As evidenced in **Fig. 2b** by the shift of the (100) diffraction peak of the α-phase to higher diffraction angles post-annealing, leading to a residual stress of - 0.7 GPa. Finally, **Fig.2c-d** and **Fig.2e-f** show SEM micrographs of the W-film before and after annealing, respectively. Micrographs are given for both surfaces (c and e) and cross-sections (d and f). Only a slight change in surface

morphology is observed. The annealed W film exhibits a dense compact morphology with an average grain size of approximately 160 ± 30 nm, determined from SEM images acquired with an AsB detector and analyzed using ImageJ. The surface roughness, measured by atomic force microscopy (AFM), is approximately 1.64 nm (root mean square, RMS). Further details are available in the supplementary materials. **Section B**.

3.2. Elastic-plastic properties of the annealed W films

The elastic modulus and hardness of a 1000 nm thick annealed α-phase W film were determined by nanoindentation using a matrix of 16 indents. **Fig. 3** shows a variation of the elastic modulus, derived using the Hay and Crawford model **[50]**, as a function of penetration depth. The modulus is very stable throughout the indentation depth, showing that the Hay and Crawford correction is working appropriately, leading to a value of ~ 360 GPa in agreement with the bulk value. The hardness of tungsten was extracted at a depth of 100 nm, representing 10 % of the film's thickness, giving a value of ~ 14 GPa. As for the modulus, there is limited size dependency up to 400 nm penetration depth. In order to identify the hardening law to be used in the finite element models, the hardness was converted into a representative flow stress associated to ~ 0.08 plastic strain, according to Kermouche's analysis **[51]**, yielding a value of 5.3 GPa. The strain hardening exponent is not known, as the film breaks in a brittle manner, making it impossible to deform specimens in uniaxial tension into the plastic regime. Nanocrystalline metals are known to exhibit small strain hardening capacity **[55]**, and the value n = 0.1 was arbitrarily selected as an upper bound. In any case, such a relative value has a limited impact on the results presented hereafter. Based on the yield stress of 5.3 GPa at a plastic strain of 0.08, one extracts the initial yield stress σ_0 = 4.3 GPa.

3.3. Fracture toughness analysis

Over 90 stable crack-on-chip test structures of annealed 370 nm α-phase W films were examined by SEM to measure the lengths of the arrested cracks. **Fig. 4a** and **b** show SEM images of two successful COC test structures featuring a starter notch of length a_0 = 3 μm and markedly different crack extensions equal to (a) ≈ 1.2 μm and (b) ≈ 5.3 μm, respectively, associated to different actuator lengths of 16.2 μm and 31.1 μm respectively. The fracture toughness for each of the experimentally measured crack extensions has been determined with the 2D elastic plane stress finite element model for static crack **[40]** (see **Fig. 4c**). Each structure was replicated with identical parameters, including geometry, crack extension, and residual stresses in addition to Young's modulus and Poisson's ratio of both the W specimen and the SiN actuator films. For all structures, which had varying actuator beam and notch lengths, the crack extensions Δa ranged from 0.2 to 13 μm, as shown in **Fig. 4d** along with the calculated K_{Ic} values. No obvious correlation could be found between the COC dimensions, actuator length, starter notch length and Δa with K_{Ic} suggesting that the large variability may have a different origin, as discussed later in **Section 4**. In any case, generating 90 successful crack arrest tests on submicron specimens to be analyzed through rigorous fracture mechanics was a key milestone for this research.

Fig. 4d illustrates that most data points are clustered around crack extensions between 0.5 and 2 μm (see dashed black box), corresponding to fracture toughness values ranging from 2.5 to 4 MPa√m. The fracture toughness values derived from the 90 COC test structures result in an average K_{Ic} equal to 3.20 ± 0.36 MPa√m.

3.4. Failure mechanisms

Fig. 5 presents SEM micrographs of three successful W COC test structures, each illustrating distinct crack behaviors and morphologies. In **Fig. 5a**, the crack deviates from a linear path relative to the notch tip, suggesting that the propagation is influenced by the grain morphology

typical of an intergranular cracking mechanism. **Fig. 5b** reveals a different behavior, where two short cracks initiate and propagate independently from two separate locations at the notch tip. Finally, **Fig. 5c** displays a crack that grows at an angle towards one side of the specimen, after initiating from the notch.

Fig. 6 shows an SEM micrograph of a propagating crack in a COC test structure, accompanied by zoomed-in images of the crack surfaces. The intergranular cracking mechanism is confirmed. More evidence about the intergranular nature of the crack propagation is provided in the supplementary materials (**Fig. C2**). The close-ups reveal that the surfaces are not sharp and do not align perfectly if they were to be brought back together. This indicates some degree of plastic distortion accompanying the failure process at the grain boundaries.

In order to ensure an accurate measurement of the crack extension (Δa) and to confirm the absence of any significant crack front inclination through the thickness of the W specimen, we compared the crack lengths measured on both sides of some specimens. To this end, a focused ion beam (FIB) was utilized to section the W test specimen, enabling measurement by looking at the crack length on the bottom side. This measurement was then compared to the corresponding value obtained from the top surface. **Fig. 7** presents SEM micrographs of a COC test structure: **(a)** before FIB sectioning, showing the top surface, and **(b)** after FIB sectioning, showing the bottom surface. Careful analysis of the two micrographs using ImageJ ® software indicates that the crack length on the bottom face of the COC test structure is slightly longer than that at the top surface (1.63 μm vs. 1.61 μm), with a difference of 20 nm (≈ 1.2 %) within experimental uncertainty. The same procedure was applied to a second COC test structure with a longer crack, yielding a top surface crack length equal to 10.97 μm and a bottom surface crack length of 11.10 μm, resulting in a difference of 130 nm (≈ 1.2%) which is close again to the precision of crack length measurement. Further details about the FIB preparation can be found in Appendix **Section C**.

3.5. Modelling 'R-curve' effect due to plastic dissipation

The XFEM model, based on a description of the fracture process by cohesive zone elements, was used to assess the impact of near-crack-tip plastic dissipation on the crack growth resistance and on the toughness extracted after some amount of crack growth and not at the exact time of initiation. The goal is to determine whether an 'R-curve' type behavior can be expected, with the crack resistance increasing as the crack propagates owing to increasing plastic zone size and reverse plasticity in the crack wake.

Given the average fracture toughness value of 3.2 MPa√m and the yield strength of 4.3 GPa, a simple analytical calculation of the plastic zone size r_p (plane strain) gives a value of ~ 50 nm, which is only about 10 % of the film thickness. Therefore, the plane strain assumption made in the numerical model is a priori justified by the fact that the material surrounding the plastic zone behaves as an almost rigid body, preventing any through-thickness plastic contraction (hence plane strain) from the perspective of the crack tip. This is checked a posteriori hereafter.

The mesh was very refined in the central part of the sample where the crack propagates, with an element size of about 1 nm size and XFEM enrichment. Convergence with respect to the mesh discretization was confirmed by running simulations with different element sizes up to 3 nm providing exactly the same arrest crack length at equilibrium. **Figure 8** shows two snapshots of the near crack fracture process zone corresponding to a calculation with peak stress $\hat{\sigma}$ equal to 7.8 GPa and Γ_0 equal to 26 J/m^2 (see later for the choice of these values) and 1 nm element size. The coloring indicates elements that are active in the FPZ. A value of 1 "red" means a completely broken element with the Abaqus indicator "status XFEM". **Fig. 8a** corresponds to the crack just after initiation. The FPZ length is equal to 10 nm. **Fig. 8b** shows the near crack tip at crack arrest with FPZ length now equal to 25 nm. Convergence is reached because enough elements are included in the FPZ to resolve the large variations of the stress during the failure process. This is a very important point in this study. The possibility to use such fine meshes is

very much facilitated by the use of microscopic specimens compared to cm-sized specimens and the convergence is facilitated by the XFEM method

Hundreds of simulations were conducted in order to identify the parameters of the traction separation law that would allow the reproduction of the experimental values. Each simulation is characterized by different pairs of peak strength $\hat{\sigma}$ and Γ_0 as input parameters, with the measured crack extension as output. The peak stress was varied between σ_0 and $2\sigma_0$ meaning in this case between 5 and 10 GPa, while Γ_0 was adjusted to induce crack propagation. To allow this refined mesh in the crack path without meshing the entire specimen with such very small elements, the crack extensions were limited to a maximum of 2 µm, which corresponds to the majority of the experimentally measured extensions (highlighted in a black dashed box in **Fig. 4d**).

Fig. 9a shows a map of the measured crack extensions Δa in the space of the imposed $\hat{\sigma} - \Gamma_0$. Interestingly, for a given fracture energy Γ_0, the range of peak stresses $\hat{\sigma}$ that results in the experimental Δa values is narrow, and vice versa. This finding suggests that small local variations of $\hat{\sigma}$ and/or of $,\Gamma_0$, likely due to small variation in the tungsten nanostructure, can significantly influence the crack resistance and thus the crack arrest length, potentially explaining the experimental scatter in fracture toughness values already discussed above.

Subsequently, the fracture energy values Γ_0 were analytically converted to fracture toughness values K_{Ic}, assuming no R-curve effect (i.e. $G_c = \Gamma_0 + \Gamma_p$ with $\Gamma_p \approx 0$) and using the plane strain assumption as:

$$K_{Ic} = \sqrt{\Gamma_0 \frac{E}{1-\nu^2}} \quad . \tag{4}$$

Fig. 9b shows the resulting $\hat{\sigma} - K_{Ic} - \Delta a$ map, with K_{Ic} values ranging from 2.8 to 3.6 MPa√m. Remarkably, the fracture toughness values obtained under the assumption of no

R-curve effect perfectly match those obtained using the 2D purely elastic model in **Section 3.3**, with $K_{Ic} = 3.2 \pm 0.36$ MPa√m. This confirms that any R-curve effect due to plastic dissipation at the crack tip is minor in the case of the nanostructured W film and may only contribute to the experimental scatter in the fracture toughness values. This comes from the nature of the quasi-brittle fracture mechanism taking place at the grain boundaries with a strength reflected by $\hat{\sigma}$, being significantly lower than $3\sigma_0$. As shown in a vast literature about crack propagation simulation with a CZM, plastic dissipation remains modest as long as $\hat{\sigma} < \alpha\sigma_0$ with α typically equal to 3 but depending on *n* and on the crack configuration **[56]**.

Finally, the plane strain assumption based on the size of the plastic zone can be verified. **Fig. 9c** shows the equivalent plastic strain at the crack tip (with a crack extension of 1 μm) in its crack arrest configuration after the release of residual stresses in the actuator for a parameter set of $\hat{\sigma} = 7.8$ GPa and $\Gamma_0 = 26$ J/m² (≈ 3.2 MPa√m). The radius of the plastic zone is 23 nm, i.e. only 6 % of the film thickness, which is small enough to ensure plane strain conditions.

4. Discussion

4.1. On the validity of K_c and on the sources of uncertainty

4.1.1. Geometric and elastic parameters

A primary source of error in the determination of K_c arises from the uncertainties in the experimental measurement of the geometric parameters of the COC test structures and/or from the elastic properties that are introduced in the FE models. Systematic errors can occur during SEM, profilometry or nanoindentation measurements, potentially exceeding 10 %. An error propagation analysis was conducted to evaluate the impact of these uncertainties on K_c. This analysis assessed the contribution of each measured parameter included in the FE simulations based on the following analytical formula **[40]** for *K* corresponding to the COC test structures with sufficiently long cracks (double cantilever type geometry):

$$K = (1 - \nu_a)\, \sigma_a^{int} \sqrt{L_a}\, \frac{8\sqrt{3(1-\nu^2)\frac{L_a}{L}}}{16\frac{E_a}{E}\left(\frac{a}{L}\right)^2 + \frac{L}{a}\frac{L_a}{W_a}\frac{t}{t_a}}, \quad (5)$$

where L_a, W_a, t_a, E_a, ν_a, σ_a^{int} are the length, width, thickness, elastic modulus, Poisson ratio, and internal stress of the SiN actuator beams, respectively, L, t, E, ν are the length, thickness, elastic modulus, and Poisson ratio of the test specimen, respectively, and a is the crack length. The standard deviations on the measurements of each of these independent parameters lead to the estimation of a total error on K_c between 11 % and 12 %, when the fracture toughness is determined using the 2D elastic plane stress model as described in **Section 3.3**.

4.1.2. Crack propagation behavior

Another source of variation of K_c can be attributed to the crack propagation behavior, which does not always ideally proceed along a straight line.

Firstly, the microstructure of the nanostructured W film is characterized by a high density of grain boundaries. The crack follows the grain boundaries as shown in **Fig. 5a.** The GB's can either facilitate crack propagation by acting both as stress concentration sites and lower energy interfaces with lower strength than the grains interior or hinder it by forcing the crack to follow a tortuous path along the grain boundary pattern inducing some mode II local contribution. This variability in the crack path can result in different degrees of shielding, leading to varying fracture toughness values across different COC test structures, for further SEM illustrations **see section C** of the supplementary material. This behavior is consistent with the results of previous studies, such as **[23]**, which reported similar scatter on K_c of ultra-fine-grained (average grain size of 790 nm) W microcantilevers at room temperature. The authors found a variation in the measured K_c from 3.8 to 5.1 MPa√m and attributed the variations to crack initiation occurring in one or two crystallographically favourable grains or along grain boundaries. The fracture surface revealed a mixture of transcrystalline and intercrystalline crack propagation across

multiple grains and grain boundaries, explaining the observed scatter. Here, the impact would be on setting the arrest crack length a little shorter or a little longer, depending on the specific crystallography of the grains screened by the running crack when the energy release rate gets close to the critical value. Another study **[57]** investigating the fracture toughness of 0.1 mm thick W foil with a crack perpendicular to the elongated grains (~ 400 nm in the transverse direction) at room temperature demonstrated significant scatter, ranging from 20 to 110 MPa√m. The fracture surface morphology varied, with cleavage fracture corresponding to the lowest fracture toughness values and delamination corresponding to the highest values.

Secondly, due to microfabrication artifacts, the details of the notch tip geometry exhibit some variability resulting in variable stress concentrations along the notch front. This variability affects the crack initiation dynamics, resulting in partly different crack propagation histories, sometimes with multiple nano cracks initiating from different locations on the notch tip, as shown in **Fig. 5b.** The redistribution of stress concentration at the notch tip between two cracks instead of one can affect the final crack length as well as the fracture toughness values. For sufficiently long Δa, these effects should not affect too much the crack arrest but for short Δa these effects cannot be discarded.

Thirdly, in addition to the notch effect, misalignment artefacts could bias crack propagation towards one side of the specimen, as shown in **Fig. 5c**, causing variability in crack lengths and fracture toughness values for different COC test structures.

A fourth source of error may result from some degree of crack inclination through the coating thickness, causing differences in the crack length when looking at the two opposite surfaces. However, based on the observations made in **Fig. 7** only a slight difference in crack length was found between the top and bottom surfaces of the W specimen, with the bottom surface being approximately 1.2% longer. Given the columnar microstructure of the W films throughout their thickness, it is unlikely that the crack length would differ substantially between the top and

bottom surfaces, as the crack preferentially propagates along grain boundaries, as discussed previously which supports the reliability of the top surface crack extension measurements for accurate fracture toughness determination.

As a final sanity check, 3D simulations were performed with a static crack using linear elasticity to challenge the predictions of the 2D plane stress model. The J integral values agree perfectly between the two models. Comparative simulations were also conducted using the elastic 2D static crack model under both plane stress and plane strain conditions for the test specimen. The results indicated that the calculated fracture toughness value under plane strain conditions is 7 % higher than that under plane stress conditions, this validates the extracted K_c values.

4.2. Fracture toughness of W-thin film versus bulk

Fracture toughness studies on miniaturized W specimens, predominantly using focused ion beam (FIB)-fabricated micro-cantilever beams, have reported a broad range of values depending on material type, scale, and analysis method, see introduction. For tungsten single crystals, Wurster et al. **[34]** reported values between 2.9 and 3.7 MPa√m using linear elastic fracture mechanics (LEFM), 12.5 to 22.3 MPa√m when based on the J-integral and elastoplastic analysis, and 9.2 to 14.4 MPa√m using the critical crack tip opening displacement. Ast et al. **[35]** investigated the size effect affecting the fracture toughness (FT) of as-received and pre-strained W single-crystal cantilevers. They reported minimum fracture toughness values as low as 1.5 MPa√m in the smallest W cantilevers using LEFM, while slightly larger cantilevers exhibited values around 3.31 MPa√m. Values between 5.5 to 6.6 MPa√m were reported, using EPFM. Similarly, Bohnert et al. **[58]** addressed the fracture toughness of W single-crystal through numerical finite element simulations and experimental methods, revealing values equal to 12.9, 13.3, and 7.6 MPa√m using FE-based cohesive zone modelling, J-integral, and LEFM, respectively. It is worth noting that the W cantilevers in this last study were much larger than

those tested in previous studies. Extending to polycrystalline W specimens, Wurmshuber et al. **[59]** evaluated the toughness of ultrafine-grained (UFG) W (140–160 nm, prepared via high-pressure torsion) using size-varied notched cantilevers and EPFM J-integral analysis. Fracture toughness ranged from 12 MPa√m for smaller beams to 30 MPa√m for larger ones. Furthermore, in **[35]** a value of 6.5 MPa√m was reported for an ultrafine-grained W specimen with an average grain size of 790 nm. Subsequently, Fritze et al. **[60]** evaluated the fracture toughness of 4.5 µm magnetron sputtered W films using notched micro-cantilever beams and they reported fracture toughness of ~4.5 MPa√m for pure W, decreasing to 3.4 and 3.2 MPa√m with 2 and 4 at.% carbon doping, respectively.

Room-temperature fracture toughness values for bulk pure W with millimetre-scale dimensions vary widely, depending on processing methods and resulting microstructures. Rupp and Weygand **[11]** measured K_c values of 13.4 MPa√m and 8.1 MPa√m for polycrystalline W rods (produced by powder metallurgy and 65% rolling) for the crack propagation direction parallel and perpendicular to the rolling direction, respectively. The material featured elongated grains (aspect ratio ~1:3) and subgrains of a size that is less than 1 µm, aligned along the rolling direction. In a separate study, Gludovatz et al. **[61]** studied ultrafine-grained and potassium-doped W processed via severe plastic deformation (high-pressure torsion), achieving grain sizes of ~100 nm. They reported higher K_c values of 35 MPa√m for pure W and 32.06 MPa√m for potassium-doped W (1 mm rods), while coarse-grained specimens (≥4 mm) showed significantly lower toughness (5–10 MPa√m). Similarly, Faleschini et al. **[32]** studied pure tungsten (99.98%) produced via powder metallurgy in as-sintered and rolled conditions, both exhibiting grain sizes of several micrometers. Fracture toughness was approximately equal to 5 MPa√m for sintered specimens and 5.4 MPa√m for rolled ones. Following severe plastic deformation (SPD), the grain size was refined to ~300 nm, resulting in a fracture toughness of ~30 MPa√m. Additionally, Murphy et al. **[62]** investigated W films produced by chemical vapor

deposition (CVD), yielding a columnar grain structure (10 μm wide, 10–200 μm long). Fracture toughness measured by four-point bending was approximately 5 MPa√m for notches parallel and 4 MPa√m for notches perpendicular to the growth direction.

Reviewing the reported studies on the fracture toughness of W, it is evident that the wide range of measured values arises from multiple factors. These include specimen size effects, microstructural differences, as well as variations in failure mechanisms. Each of these factors contributes to the observed discrepancies in K_c values. Regarding specimen size effects, the fracture toughness can potentially increase as the thickness of the test specimen increases because of the near plane stress conditions, reach a peak value, and then decrease with a further increase in thickness, This transition regime between plane stress and plane strain is different from one material to another and it depends on both the strength and toughness of the material that decisively controls the thickness regime dominated by near plane stress conditions **[63]**.

In the case of the present W nanostructured films, near-plane stress conditions would require thicknesses below 50-100 nm (thinner than tested here) to have a plastic zone size similar to the film thickness **[63]**. In other words, no size effect can be expected in the present context. If the yield stress decreases by a factor 3 and FT increases by a factor 2, the plastic zone size would be around 2 to 4 micrometers, putting microcantilevers of the literature also in the plane strain regime. Finally, aside from the plane stress/plane strain transition, other sources of constraint effects can play a role if the specimen dimensions are not large enough, leading to a drop of stress triaxiality at the crack tip. Such effects can be important for ductile fracture mechanisms, but are out of the present scope. Hence, true specimen size effects can be discarded (except for conditions of very large K_c of W).

Regarding failure mechanisms, fracture toughness varies between transgranular cleavage, primarily observed in single crystals and intergranular fracture in tungsten polycrystals, with delamination ductile failure in some cases as in **[57]**. Notably, brittle cleavage

has been reported in ultrafine-grained (UFG) tungsten (790 nm grain size) tested with a submicron specimen **[35]**. The present results are relevant only within the context of an intergranular (brittle) fracture mechanism. An interesting observation emerges when comparing previous studies on W cantilever-free beams prepared from PVD **[60]** and CVD **[62]** coatings. In both cases, intergranular (inter-columnar) failure was observed, with comparable K_c values of 4.5 and 5 MPa√m, respectively, despite the PVD coating being 4.5 μm thick and the CVD coating 1 mm thick. Intergranular/intercolumnar fracture in nanostructured metallic thin films can be purely brittle, occurring by intergranular fracture when the material's yield strength is excessively high due to nano-sized grains or because of grain boundary embrittlement due to impurities residing at this level. Alternatively, the fracture can be intergranular ductile, resulting from the coalescence of voids nucleated along well-oriented grain boundaries, potentially leading to their decohesion, owing to lower yield strength, which allows for more plastic deformation **[55]**. In some cases, the two mechanisms could co-exist depending on the thickness of the test film, as reported in **[64]** on sputter-deposited Cu films or on the impurities level at the grain boundaries, as found for sputter-deposited Al films **[65]**. In any case, the present $\Gamma_0 \approx 26\,\mathrm{J/m^2}$ is too high for a pure cleavage mechanism. The crack morphology in our COC test structures **(Fig.6)** appears more as a combination of brittle intergranular fracture with some ductile events including sparse void nucleation and some degree of plastic distortion.

Finally, regarding microstructure, texture effects/ grain morphology **[11, 61, 66]**, impurities segregations at GB **[37, 67]**, dislocation density **[68]**, and grain size **[61, 62]** are the main parameters that can affect the FT. In the present study, the dominant parameter is certainly the grain size (~ 160 nm). This small grain size leads to yield strength levels above 4 GPa compared to 1 to 1.3 GPa in bulk W with micrometre-size grains **[69]**. This means that if the identified peak stress of the traction separation zone equal to 7.8 GPa is a correct estimation of the strength of the fracture process zone for grain boundary failure independent of grain size

(i.e. this assumes nominally similar GB and GB chemistry) the ratio $\frac{\hat{\sigma}}{\sigma_0}$ in bulk W would be close to 4. Such a ratio can then lead to a significant R-effect, absent when $\frac{\hat{\sigma}}{\sigma_0}$ is below 3 as in our thin film specimens. Combined with the fact that many bulk tests are based on not-fatigue pre-cracked specimens, one can expect that the measured K_c is affected by an R-effect, more crack tip plastic deformation and thus extra dissipation contributing to having a G_c in bulk form is equal to ~ 100 J/m^2 to be compared to ~ 28 J/m^2. Now, the fact that the present film structure is columnar probably also plays a role in limiting the possible toughening by crack deflection, which is difficult to assess quantitatively.

The cohesive zone approach has been used to rationalize the present results and justify that the K_c values obtained at crack arrest can be safely compared to K_c extracted at initiation. Otherwise, the methodology would have provided an inverse identification of K_c at initiation based on Γ_o. Furthermore, this model also allows linking with the differences to be expected with bulk specimens. Further analysis is needed to consolidate this finding, but if it is correct, it directly opens an avenue for the transferability of the nano- or micro-scale specimen results to macroscopic components. Similar to the transfer of ductile or cleavage fracture laboratory data to components by the local approach to fracture **[70]**, a similar approach can be followed with the CZM model here describing the intergranular failure mode. The underlying idea is that once the parameters of the traction separation law are identified, they can be used independently of the geometry as long as the failure mechanism does not change, i.e. remains in the brittle intergranular regime. The transfer would remain valid even if the plastic properties vary as a result, for instance, to a change of grain size, texture, or dislocation density, considering that these changes are properly considered when modelling the plasticity.

5. Conclusion

The fracture toughness of freestanding 370 nm-thick nanostructured tungsten films, deposited via magnetron sputtering, has been determined with an on-chip fracture mechanics test method, complemented by finite element modelling. These models included both 2D and 3D static J-integral analyses, as well as extended finite element method (XFEM) simulations relying on a cohesive zone model to represent the failure process. The study led to the following findings:

- The crystal phase, morphology, and residual stress levels in magnetron-sputtered tungsten films significantly vary with the deposition parameters, specifically the working gas pressure. Care should then be taken to generate films that are the most representative of the tungsten α-phase.
- High compressive residual stress in sputter-deposited α-phase tungsten complicates the execution of reliable on-chip cracking tests, requiring an annealing heat treatment to reduce their magnitude.
- The fracture toughness of α-phase W films is equal to $K_c = 3.2 \pm 0.36$ MPa$\sqrt{\text{m}}$, meaning $G_c \approx 28.3 \pm 3.6\ \text{J/m}^2$ aligning with previously reported data extracted from W micro-cantilever under linear elastic fracture mechanics (LEFM) conditions. This value is about 50% of the lowest fracture toughness reported for bulk W at room temperature for similar quasi-brittle intergranular mechanisms.
- The fracture process zone behavior can be represented by a traction separation law with fracture energy $\Gamma_0 \approx 26\ \text{J/m}^2$ and a peak strength $\hat{\sigma} = 7.8$ GPa to reproduce the experimental results. These characteristics lead to limited R-curve effect on the cracking of the thin film specimens, hence $G_c \approx \Gamma_0$, indeed. With $\sigma_0 = 4.3\ GPa$, the ratio $\frac{\hat{\sigma}}{\sigma_0}$ is equal to 1.8, explaining the absence of significant plastic dissipation. In bulk form, σ_0

is much lower, with $\frac{\hat{\sigma}}{\sigma_0}$ then being larger than 3, that can explain more significant plastic dissipation and higher fracture toughness.

- The cohesive zone model approach offers thus a path to transfer laboratory data obtained on nano or micro-scale specimens to macroscopic components assuming the failure mechanism is the same. For intergranular fracture, this implies that the grain boundaries must have the same characteristics and composition. The possible change of plastic behavior can be taken into account through changing the hardening law and constitutive model.

The next step in this research effort is the application of ion irradiation to W films, combined with transmission electron microscopy. The advantage of using thin films is to enable relatively homogenous doses over the thickness of the specimen. This is crucial for optimizing the performance of W coatings as well as bulk W components to be used in future nuclear fusion power reactors, even though testing on neutron irradiated specimens will ultimately remain necessary such as with the IFMIF-DONES facility under development **[71,72]**.

Authors contributions:

S.E. Naceri: Research execution, experimental work, 2D finite element (FE) modelling, results discussion, and original manuscript drafting. M. Rusinowicz: XFEM-CZM simulations conduction, writing, and contribution to the discussion of the results. M. Coulombier: Microfabrication mask design, process development, and FIB preparation. T. Pardoen: Supervision, conceptualization of the study, discussion of results, and manuscript writing, review and improvement. All authors have reviewed and approved the final version of the manuscript for submission.

Acknowledgement:

The authors sincerely thank the Winfab cleanroom staff at UCLouvain for their support in the microfabrication processes and Dr Nicolay Tumanov from the PC2 platform at UNamur for his valuable assistance with the GIXRD characterization.

References

[1] ITER. The Way to New Energy. 2021. Available online: http://www.iter.org/ (accessed on 15 April 2023)

[2] Federici, G., Bachmann, C., Barucca, L., Biel, W., Boccaccini, L., Brown, R., Bustreo, C., Ciattaglia, S., Cismondi, F., Coleman, M., Corato, V., Day, C., Diegele, E., Fischer, U., Franke, T., Gliss, C., Ibarra, A., Kembleton, R., Loving, A., . . . You, J. (2018). DEMO design activity in Europe: Progress and updates. *Fusion Engineering and Design*, *136*, 729-741. https://doi.org/10.1016/j.fusengdes.2018.04.001

[3] Stork, D., Heidinger, R., Muroga, T., Zinkle, S. J., Moeslang, A., Porton, M., ... & Ibarra, A. (2017). Towards a programme of testing and qualification for structural and plasma-facing materials in 'fusion neutron'environments. *Nuclear Fusion*, *57*(9), 092013 http://doi.org/10.1088/1741-4326/aa60af

[4] J. Knaster, A. Moeslang, T. Muroga, Materials research for fusion, Nature Phys., 12 (2016) 424–434. https://doi.org/10.1038/nphys3735

[5] T. Zhang, Z. Xie, C. Liu, Y. Xiong, The Tungsten-Based Plasma-Facing Materials, IntechOpen, New York, 2020. https://doi.org/10.5772/intechopen.88029

[6] S. Wang, W. Guo, Y. Yuan, N. Gao, X. Zhu, L. Cheng, X. Cao, E. Fu, L. Shi, F. Gao, G. Lu, Evolution of vacancy defects in heavy ion irradiated tungsten exposed to helium plasma, J. Nucl. Mater., 532 (2020) 152051. https://doi.org/10.1016/j.jnucmat.2020.152051

[7] Lassner, E., & Schubert, W.-D. (1999). *Tungsten: Properties, Chemistry, Technology of the Elements, Alloys, and Chemical Compounds*. Springer Science & Business Media, New York.

References (main text)

[8] Zhang, Y., Ganeev, A. V., Wang, J. T., Liu, J. Q., & Alexandrov, I. V. (2009). Observations on the ductile-to-brittle transition in ultrafine-grained tungsten of commercial purity. *Materials Science and Engineering: A*, *503*(1–2), 37–40. https://doi.org/10.1016/j.msea.2008.07.074

[9] Reiser, J., Hoffmann, J., Jäntsch, U., Klimenkov, M., Bonk, S., Bonnekoh, C., & Mrotzek, T. (2016). Ductilisation of tungsten (W): On the shift of the brittle-to-ductile transition (BDT) to lower temperatures through cold rolling. *International Journal of Refractory Metals and Hard Materials*, *54*, 351–369. https://doi.org/10.1016/j.ijrmhm.2015.09.001

[10] Yan, Q., Zhang, X., Wang, T., Yang, C., & Ge, C. (2013). Effect of hot working process on the mechanical properties of tungsten materials. *Journal of Nuclear Materials*, *442*(1–3), S233–S236. https://doi.org/10.1016/j.jnucmat.2013.01.307

[11] Rupp, D., & Weygand, S. M. (2010). Anisotropic fracture behaviour and brittle-to-ductile transition of polycrystalline tungsten. *Philosophical Magazine*, *90*(30), 4055–4069. https://doi.org/10.1080/14786435.2010.504198

[12] Zhang, X., Liu, J., Zhu, X., & Wu, Y. (n.d.). Effect of laser powder bed fusion process parameter on the microstructure and properties of pure tungsten. *Available at SSRN*. https://doi.org/10.2139/ssrn.5085129

[13] T. Zhang, Z. Xie, C. Liu, Y. Xiong, The Tungsten-Based Plasma-Facing Materials, IntechOpen, New York, 2020. https://doi.org/10.5772/intechopen.88029

[14] S. Wang, J. Li, Y. Wang, X. Zhang, R. Wang, Y. Wang, J. Cao, Thermal damage of tungsten-armored plasma-facing components under high heat flux loads, Sci. Rep., 10 (2020) 1–10. https://doi.org/10.1038/s41598-020-57852-8

References (main text)

[15] S. Nogami, A. Hasegawa, M. Fukuda, M. Rieth, J. Reiser, G. Pintsuk, Mechanical properties of tungsten: Recent research on modified tungsten materials in Japan, J. Nucl. Mater., 543 (2021) 152506. https://doi.org/10.1016/j.jnucmat.2020.152506

[16] G. Pintsuk, I. Bobin-Vastra, S. Constans, P. Gavila, M. Rödig, B. Riccardi, Qualification and post-mortem characterization of tungsten mock-ups exposed to cyclic high heat flux loading, Fusion Eng. Des., 88 (2013) 1858–1861. https://doi.org/10.1016/j.fusengdes.2013.05.091

[17] V. Budaev, Y. Martynenko, A. Karpov, N. Belova, A. Zhitlukhin, N. Klimov, V. Podkovyrov, V. Barsuk, A. Putrik, A. Yaroshevskaya, R. Giniyatulin, V. Safronov, L. Khimchenko, Tungsten recrystallization and cracking under ITER-relevant heat loads, J. Nucl. Mater., 463 (2015) 237–240. https://doi.org/10.1016/j.jnucmat.2014.11.129

[18] G. Pintsuk, M. Bednarek, P. Gavila, S. Gerzoskovitz, J. Linke, P. Lorenzetto, B. Riccardi, F. Escourbiac, Characterization of ITER tungsten qualification mock-ups exposed to high cyclic thermal loads, Fusion Eng. Des., 98-99 (2015) 1384–1388. https://doi.org/10.1016/j.fusengdes.2015.01.037

[19] Z. Sun, Q. Li, W. Wang, J. Wang, X. Wang, R. Wei, C. Xie, G. Luo, T. Hirai, F. Escourbiac, S. Panayotis, Post examination of tungsten monoblocks subjected to high heat flux tests of ITER full-tungsten divertor qualification program, Fusion Eng. Des., 121 (2017) 60–69. https://doi.org/10.1016/j.fusengdes.2017.06.009

[20] J. You, H. Greuner, B. Böswirth, K. Hunger, S. Roccella, H. Roche, High-heat-flux performance limit of tungsten monoblock targets: Impact on the armor materials and implications for power exhaust capacity, Nucl. Mater. Energy, 33 (2022) 101307. https://doi.org/10.1016/j.nme.2022.101307

References (main text)

[21] S. Huang, Z. Pan, M. Jiang, K. Zhao, Y. Su, Lifetime measurement of a particular deep crack failure on a flat-type divertor mockup under cyclic high heat flux loading conditions, Nucl. Fusion, 62 (2022) 026040. https://doi.org/10.1088/1741-4326/ac41f7

[22] A. Durif, M. Richou, J. Bergheau, L. Gallais, G. Kermouche, G. Pintsuk, T-REX: Numerical tool for tungsten damage assessment for DEMO, J. Nucl. Mater., 569 (2022) 153906. https://doi.org/10.1016/j.jnucmat.2022.153906

[23] C. Bonnekoh, A. Hoffmann, J. Reiser, The brittle-to-ductile transition in cold rolled tungsten: On the decrease of the brittle-to-ductile transition by 600 K to −65 °C, Int. J. Refract. Met. Hard Mater., 71 (2018) 181–189. https://doi.org/10.1016/j.ijrmhm.2017.11.017

[24] Q. Wei, L. Kecskes, Effect of low-temperature rolling on the tensile behavior of commercially pure tungsten, Mater. Sci. Eng.: A, 491 (2008) 62–69. https://doi.org/10.1016/j.msea.2008.01.013

[25] J. Zhang, W. Wang, W. Ji, et al., Ultrafine Grain Tungsten Heavy Alloys with Excellent Performance Prepared by Spark Plasma Sintering, J. Wuhan Univ. Technol.-Mater. Sci. Ed., 35 (2020) 393–398. https://doi.org/10.1007/s11595-020-2269-6

[26] M.A. Yar, S. Wahlberg, H. Bergqvist, H.G. Salem, M. Johnsson, M. Muhammed, Chemically produced nanostructured ODS–lanthanum oxide–tungsten composites sintered by spark plasma, J. Nucl. Mater., 408 (2011) 129–135. https://doi.org/10.1016/j.jnucmat.2010.10.060

[27] H. Kurishita, S. Matsuo, H. Arakawa, T. Sakamoto, S. Kobayashi, K. Nakai, T. Takida, M. Kato, M. Kawai, N. Yoshida, Development of re-crystallized W–1.1%TiC with enhanced room-temperature ductility and radiation performance, J. Nucl. Mater., 398 (2010) 87–92. https://doi.org/10.1016/j.jnucmat.2009.10.015

References (main text)

[28] You, J., Mazzone, G., Visca, E., Greuner, H., Fursdon, M., Addab, Y., Bachmann, C., Barrett, T., Bonavolontà, U., Böswirth, B., Castrovinci, F., Carelli, C., Coccorese, D., Coppola, R., Crescenzi, F., Di Gironimo, G., Di Maio, P., Di Mambro, G., Domptail, F., . . . Zhang, K. (2022). Divertor of the European DEMO: Engineering and technologies for power exhaust. *Fusion Engineering and Design*, *175*, 113010. https://doi.org/10.1016/j.fusengdes.2022.113010

[29] Jin, Y. Z., Liu, X., Lian, Y. Y., & Song, J. P. (2022). Influence of recrystallization on tungsten divertor monoblock under high heat flux. *Tungsten*, *4*(3), 194-202. https://doi.org/10.1007/s42864-021-00126-1

[30] C. Yin, D. Terentyev, T. Zhang, S. Nogami, S. Antusch, C. Chang, R.H. Petrov, T. Pardoen, Ductile to brittle transition temperature of advanced tungsten alloys for nuclear fusion applications deduced by miniaturised three-point bending tests, Int. J. Refract. Met. Hard Mater., 95 (2021) 105464. https://doi.org/10.1016/j.ijrmhm.2020.105464

[31] D. Rupp, S.M. Weygand, Experimental investigation of the fracture toughness of polycrystalline tungsten in the brittle and semi-brittle regime, J. Nucl. Mater., 386 (2009) 591–593. https://doi.org/10.1016/j.jnucmat.2008.12.184

[32] M. Faleschini, H. Kreuzer, D. Kiener, R. Pippan, Fracture toughness investigations of tungsten alloys and SPD tungsten alloys, J. Nucl. Mater., 367–370 (2007) 548–551. https://doi.org/10.1016/j.jnucmat.2007.03.079

[33] A. Giannattasio, S.G. Roberts, Strain-rate dependence of the brittle-to-ductile transition temperature in tungsten, Philos. Mag., 87 (2007) 2589–2598. https://doi.org/10.1080/14786430701253197

References (main text)

[34] S. Wurster, C. Motz, R. Pippan, Characterization of the fracture toughness of micro-sized tungsten single crystal notched specimens, Philos. Mag., 92 (2012) 1803–1825. https://doi.org/10.1080/14786435.2012.658449

[35] J. Ast, M. Göken, K. Durst, Size-dependent fracture toughness of tungsten, Acta Mater., 138 (2017) 198–211. https://doi.org/10.1016/j.actamat.2017.07.030

[36] Schmuck, K., Burtscher, M., Alfreider, M., Wurmshuber, M., & Kiener, D. (2024). Micro-mechanical fracture investigations on grain size tailored tungsten-copper nanocomposites. *JOM*, *76*(5), 2302–2314. https://doi.org/10.1007/s11837-023-06348-7

[37] Tian, C., Ma, Y., Ghafarollahi, A., Patil, P., Dehm, G., Bitzek, E., ... Best, J. P. (2023). Segregation-enhanced grain boundary embrittlement of recrystallised tungsten evidenced by site-specific microcantilever fracture. *Acta Materialia*, *259*, 119256. https://doi.org/10.1016/j.actamat.2023.119256

[38] G. Dehm, B.N. Jaya, R. Raghavan, C. Kirchlechner, Overview on micro-and nanomechanical testing: New insights in interface plasticity and fracture at small length scales, Acta Mater., 142 (2018) 248–282. https://doi.org/10.1016/j.actamat.2017.06.019

[39] M. Coulombier, G. Guisbiers, M.-S. Colla, R. Vayrette, J.-P. Raskin, T. Pardoen, On-chip stress relaxation testing method for freestanding thin film materials, Rev. Sci. Instrum., 83 (2012) 105004. https://doi.org/10.1063/1.4758288

[40] S. Jaddi, Crack-on chip: A nanomechanical test method to determine the fracture toughness of thin films and 2D materials (Doctoral dissertation), Ecole Polytechnique de Louvain, UCLouvain, 2022.

References (main text)

[41] S. Jaddi, M. Coulombier, J. Raskin, T. Pardoen, Crack on a chip test method for thin freestanding films, J. Mech. Phys. Solids, 123 (2019) 267–291. https://doi.org/10.1016/j.jmps.2018.10.005

[42] S. Jaddi, J.P. Raskin, T. Pardoen, On-chip environmentally assisted cracking in thin freestanding SiO2 films, J. Mater. Res., 36 (2021) 2479–2494. https://doi.org/10.1557/s43578-021-00189-3

[43] V. Tvergaard, J.W. Hutchinson, The relation between crack growth resistance and fracture process parameters in elastic-plastic solids, J. Mech. Phys. Solids, 40 (1992) 1377–1397. https://groups.seas.harvard.edu/hutchinson/papers/420.pdf

[44] M.S. Colla, B. Amin-Ahmadi, H. Idrissi, L. Malet, S. Godet, J.P. Raskin, T. Pardoen, Dislocation-mediated relaxation in nanograined columnar palladium films revealed by on-chip time-resolved HRTEM testing, Nat. Commun., 6 (2015) 5922. https://doi.org/10.1038/ncomms6922

[45] G.G. Stoney, The tension of metallic films deposited by electrolysis, Proc. R. Soc. Lond. A, 82 (1909) 172–175. https://doi.org/10.1098/rspa.1909.0021

[46] W.C. Oliver, G.M. Pharr, An improved technique for determining hardness and elastic modulus using load and displacement sensing indentation experiments, *J. Mater. Res.*, 7 (1992) 1564–1583. https://doi.org/10.1557/JMR.1992.1564

[47] I. N. Sneddon, The relation between load and penetration in the axisymmetric Boussinesq problem for a punch of arbitrary profile, Int. J. Eng. Sci., 3(1) (1965) 47-57. https://doi.org/10.1016/0020-7225(65)90019-4

[48] K. L. Johnson, Contact Mechanics, Cambridge Univ. Press, Cambridge (1985). https://doi.org/10.1017/CBO9781139171731

References (main text)

[49] E. Meyer, Untersuchungen über Härteprüfung und Härte, Julius Springer, Berlin (1909)

[50] J. Hay, B. Crawford, Measuring substrate-independent modulus of thin films, J. Mater. Res., 26 (2011) 727–738. https://doi.org/10.1557/jmr.2011.8.

[51] G. Guillonneau, G. Kermouche, S. Bec, J.-L. Loubet, Determination of mechanical properties by nanoindentation independently of indentation depth measurement, J. Mater. Res., 27 (2012) 2551–2560. https://doi.org/10.1557/jmr.2012.261

[52] H. Sun, Z. Song, D. Guo, F. Ma, K. Xu, Microstructure and mechanical properties of nanocrystalline tungsten thin films, *J. Mater. Sci. Technol.*, 26 (2010) 87–92. https://doi.org/10.1016/S1005-0302(10)60014-X

[53] F. Vüllers, R. Spolenak, Alpha- vs. beta-W nanocrystalline thin films: A comprehensive study of sputter parameters and resulting materials' properties, *Thin Solid Films*, 577 (2015) 26–34. https://doi.org/10.1016/j.tsf.2015.01.030

[54] P. Gumbsch, Brittle fracture and the brittle-to-ductile transition of tungsten, *J. Nucl. Mater.*, 323 (2003) 304–312. https://doi.org/10.1016/j.jnucmat.2003.08.009

[55] A. Pineau, A.A. Benzerga, T. Pardoen, Failure of metals III: Fracture and fatigue of nanostructured metallic materials, *Acta Mater.*, 107 (2016) 508–544. https://doi.org/10.1016/j.actamat.2015.07.049

[56] V. Tvergaard, J.W. Hutchinson, Effect of T-stress on mode I crack growth resistance in a ductile solid, Int. J. Solids Struct., 31 (1994) 823–833. https://doi.org/10.1016/0020-7683(94)90080-9

[57] V. Nikolić, S. Wurster, D. Firneis, R. Pippan, Fracture toughness evaluation of UFG tungsten foil, Int. J. Refract. Met. Hard Mater., 76 (2018) 214–225. https://doi.org/10.1016/j.ijrmhm.2018.06.008

References (main text)

[58] C. Bohnert, N.J. Schmitt, S.M. Weygand, O. Kraft, R. Schwaiger, Fracture toughness characterization of single-crystalline tungsten using notched micro-cantilever specimens, *Int. J. Plast.*, 81 (2016) 1–17. https://doi.org/10.1016/j.ijplas.2016.01.014

[59] Wurmshuber, M., Alfreider, M., Wurster, S., Burtscher, M., Pippan, R., & Kiener, D. (2023). Small-scale fracture mechanical investigations on grain boundary doped ultrafine-grained tungsten. *Acta Materialia*, *250*, 118878. https://doi.org/10.1016/j.actamat.2023.118878

[60] Fritze, S., Hahn, R., Aboulfadl, H., Johansson, F. O., Lindblad, R., Böör, K., & Thuvander, M. (2024). Elemental distribution and fracture properties of magnetron sputtered carbon supersaturated tungsten films. *Surface and Coatings Technology*, *477*, 130326. https://doi.org/10.1016/j.surfcoat.2023.130326

[61] Gludovatz, B., Faleschini, M., Wurster, S., Hoffmann, A., & Pippan, R. (2008). Influence of microstructure on the fracture toughness of tungsten alloys. In *Refractory Metal 2008: Property of Refractory Metals* (pp. 1-6). Retrieved from https://pureadmin.unileoben.ac.at/ws/portalfiles/portal/1008984/Influence_of_Microstructure_on_the_Fracture_Toughness_of_Tungsten_Alloys.pdf

[62] Murphy, J. D., Giannattasio, A., Yao, Z., Hetherington, C. J. D., Nellist, P. D., & Roberts, S. G. (2009). The mechanical properties of tungsten grown by chemical vapour deposition. *Journal of Nuclear Materials*, *386*, 583–586. https://doi.org/10.1016/j.jnucmat.2008.12.182

[63] T. Pardoen, F. Hachez, B. Marchioni, P.H. Blyth, A.G. Atkins, Mode I fracture of sheet metal, J. Mech. Phys. Solids, 52 (2004) 423–452. https://doi.org/10.1016/S0022-5096(03)00087-5

References (main text)

[64] D.S. Gianola, B.G. Mendis, X.M. Cheng, K.J. Hemker, Grain-size stabilisation by impurities and effect on stress-coupled grain growth in nanocrystalline Al thin films, *Mater. Sci. Eng. A*, 483 (2008) 637–640. https://doi.org/10.1016/j.msea.2006.12.155

[65] N. Lu, Z. Suo, J.J. Vlassak, The effect of film thickness on the failure strain of polymer-supported metal films, *Acta Mater.*, 58 (2010) 1679–1687. https://doi.org/10.1016/j.actamat.2009.11.010

[66] Rieth, M., Dudarev, S. L., De Vicente, S. G., Aktaa, J., Ahlgren, T., Antusch, S., ... Zivelonghi, A. (2013). Recent progress in research on tungsten materials for nuclear fusion applications in Europe. *Journal of Nuclear Materials*, *432*(1–3), 482–500. https://doi.org/10.1016/j.jnucmat.2012.08.018

[67] Gludovatz, B., Wurster, S., Weingärtner, T., Hoffmann, A., & Pippan, R. (2011). Influence of impurities on the fracture behaviour of tungsten. *Philosophical Magazine*, *91*(22), 3006–3020. https://doi.org/10.1080/14786435.2011.558861

[68] Rieth, M., & Hoffmann, A. (2010). Influence of microstructure and notch fabrication on impact bending properties of tungsten materials. *International Journal of Refractory Metals and Hard Materials*, *28*(6), 679–686. https://doi.org/10.1016/j.ijrmhm.2010.04.010

[69] Y. Zhou, Y. Zhang, Y. Watanabe, Q. Xue, Microstructure and mechanical properties of tungsten–copper composites prepared by resistance sintering under ultra-high pressure, Mater. Sci. Eng. A, 475 (2008) 157–163. https://doi.org/10.1016/j.msea.2008.01.013

[70] Mudry, F. (1985). Methodology and applications of local criteria for the prediction of ductile tearing. *Elastic-Plastic Fracture Mechanics: Proceedings of the 4th Advanced Seminar on Fracture Mechanics*, Joint Research Centre, Ispra, Italy, 24–28 October 1983, in collaboration with the European Group on Fracture, 263–283. Dordrecht: Springer Netherlands. https://doi.org/10.1007/978-94-009-5380-2_10

References (main text)

[71] C. Torregrosa-Martin, A. Ibarra, J. Aguilar, F. Ambi, F. Arranz, F. Arbeiter, ... A. Zsakai, Overview of IFMIF-DONES diagnostics: Requirements and techniques, *Fusion Eng. Des*. 191 (2023) 113556. https://doi.org/10.1016/j.fusengdes.2023.113556

[72] N. García-Rodríguez, F. Canillas, F. Arranz, M. Roldán, F. Sánchez, E. Leon-Gutierrez, Study of small tensile specimen thickness effects in copper oriented for IFMIF-DONES irradiation, Nucl. Mater. Energy 39 (2024) 101679. https://doi.org/10.1016/j.nme.2024.101679

List of figures

Fig. 1. (a) SEM micrograph of a crack on-chip test structure after the release of internal stresses in the SiN actuator. (b) Zoomed-in view of the propagated crack in the W. (c) Example of a finite element model (3D J-integral) used to numerically simulate the crack-on-chip test. (d) Zoomed-in view at the crack extension

Fig. 2. (a) Residual stresses in the α and β phases of W films as a function of Ar pressure. (b) (100) diffraction peak of the α-phase before and after annealing for a deposition at an Ar pressure of 6 mTorr. (c) Corresponding SEM surface (d) cross-section image before annealing. (e) Corresponding SEM surface (f) cross-section image after annealing (taken using In-Lens detector)

Fig. 3. Results of nanoindentation tests performed on a 1000 nm thick annealed α-phase W film showing (a) the film elastic modulus and (b) the apparent hardness as a function of penetration depth

Fig. 4. SEM surface micrographs of some successful crack-on-chip test structures after the release of internal stresses in the actuator, resulting in stable arrested cracks in the tungsten films with extensions of (a) ~ 1.7 μm, for an actuator length of ~ 16.3 μm, and (b) ~ 5.3 μm for an actuator length of ~ 32.1 μm. (d) Steady-state fracture toughness as a function of crack extension, estimated using (c) the 2D plane stress elastic finite element model with the J-integral method applied to a crack of the same length as the one measured experimentally.

Fig. 5. Selected SEM micrographs of COC test structures illustrating different crack propagation behaviors leading to scatter in fracture toughness values: (a) crack deviation due to the “microstructure effect”, (b) initiation and propagation of two cracks due to the “stress state at the notch front effect”, (c) side crack propagation due to the “misalignment and notch effect”.

Figures (main text)

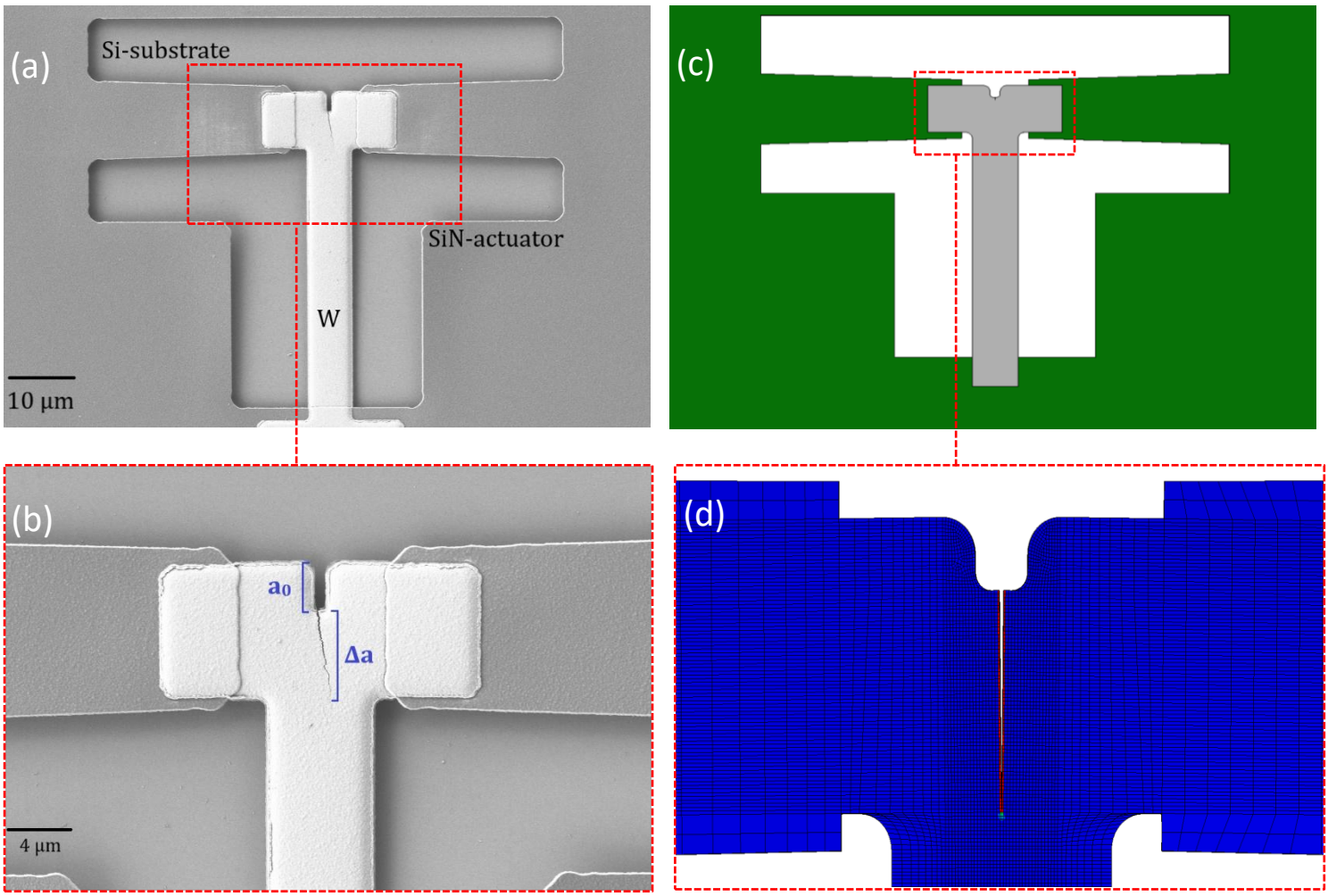

Fig. 1. (a) SEM micrograph of a crack on-chip test structure after the release of internal stresses in the SiN actuator. (b) Zoomed-in view of the propagated crack in the W specimen. (c) Example of a finite element model (3D J-integral) used to numerically simulate the crack-on-chip test. (d) Zoomed-in view of an extended crack in the FE model.

Figures (main text)

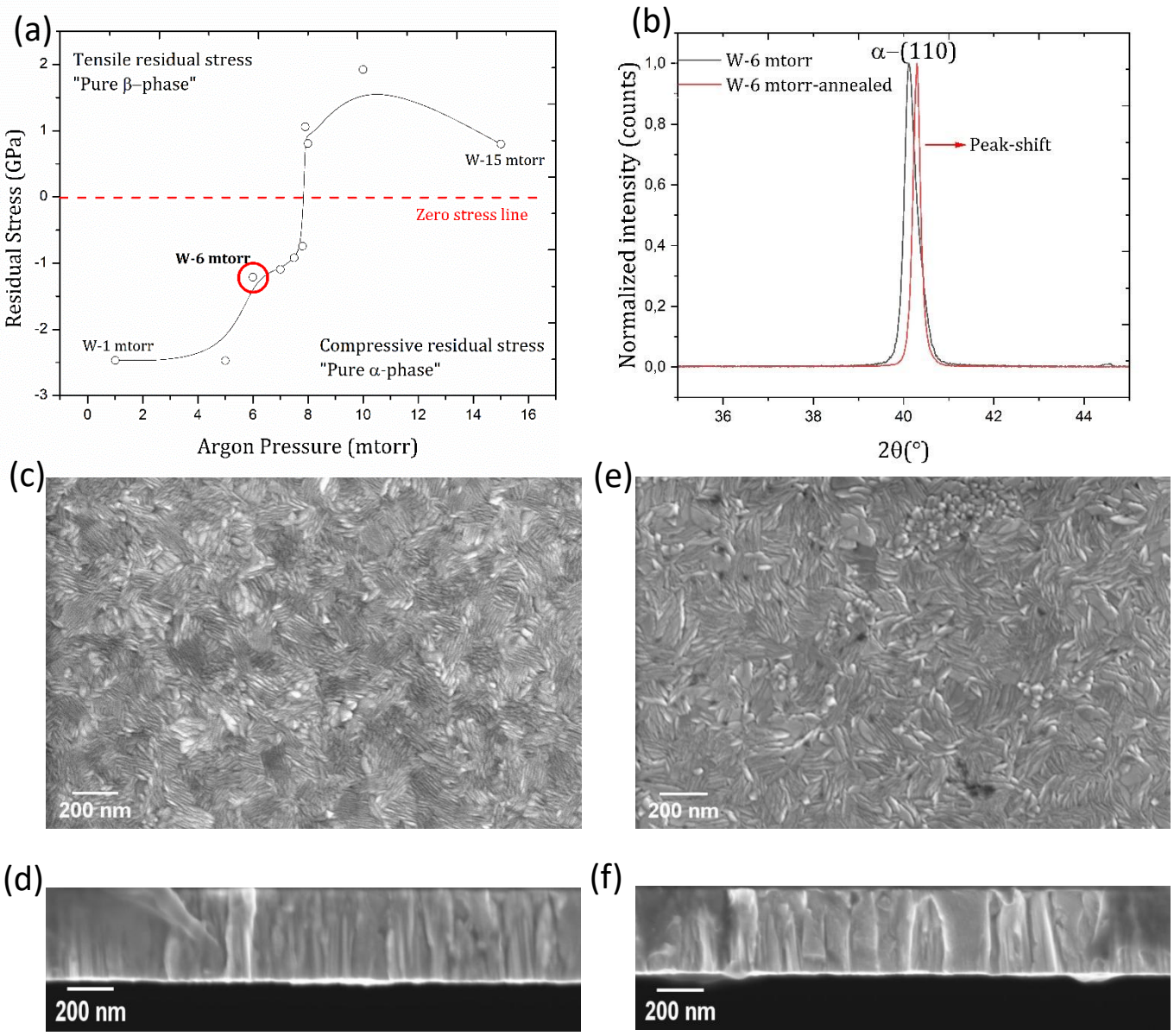

Fig. 2. (a) Residual stresses in the α and β phases of W films as a function of Ar pressure. (b) (100) diffraction peak of the α-phase before and after annealing for a deposition at an Ar pressure of 6 mTorr. (c) Corresponding SEM surface (d) cross-section image before annealing. (e) Corresponding SEM surface (f) cross-section image after annealing (taken using In-Lens detector)

Figures (main text)

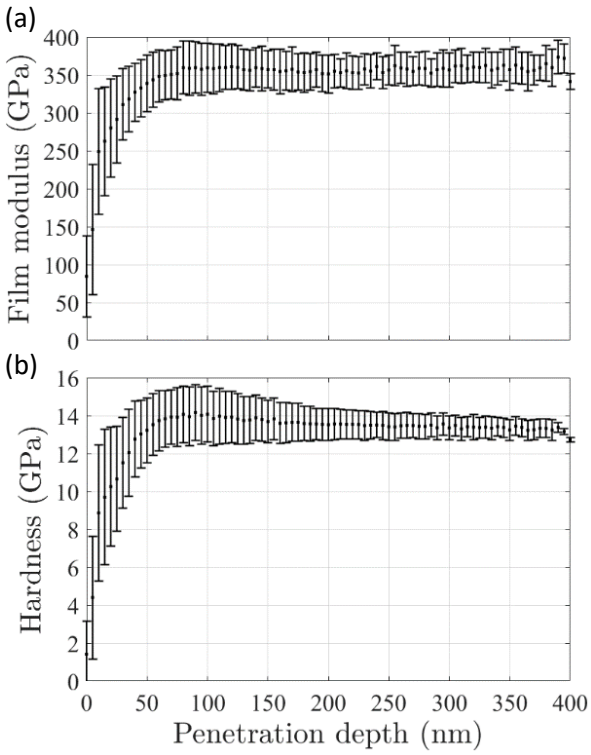

Fig. 3. Results of nanoindentation tests performed on a 1000 nm thick annealed α-phase W film showing (a) the film elastic modulus and (b) the apparent hardness as a function of penetration depth

Figures (main text)

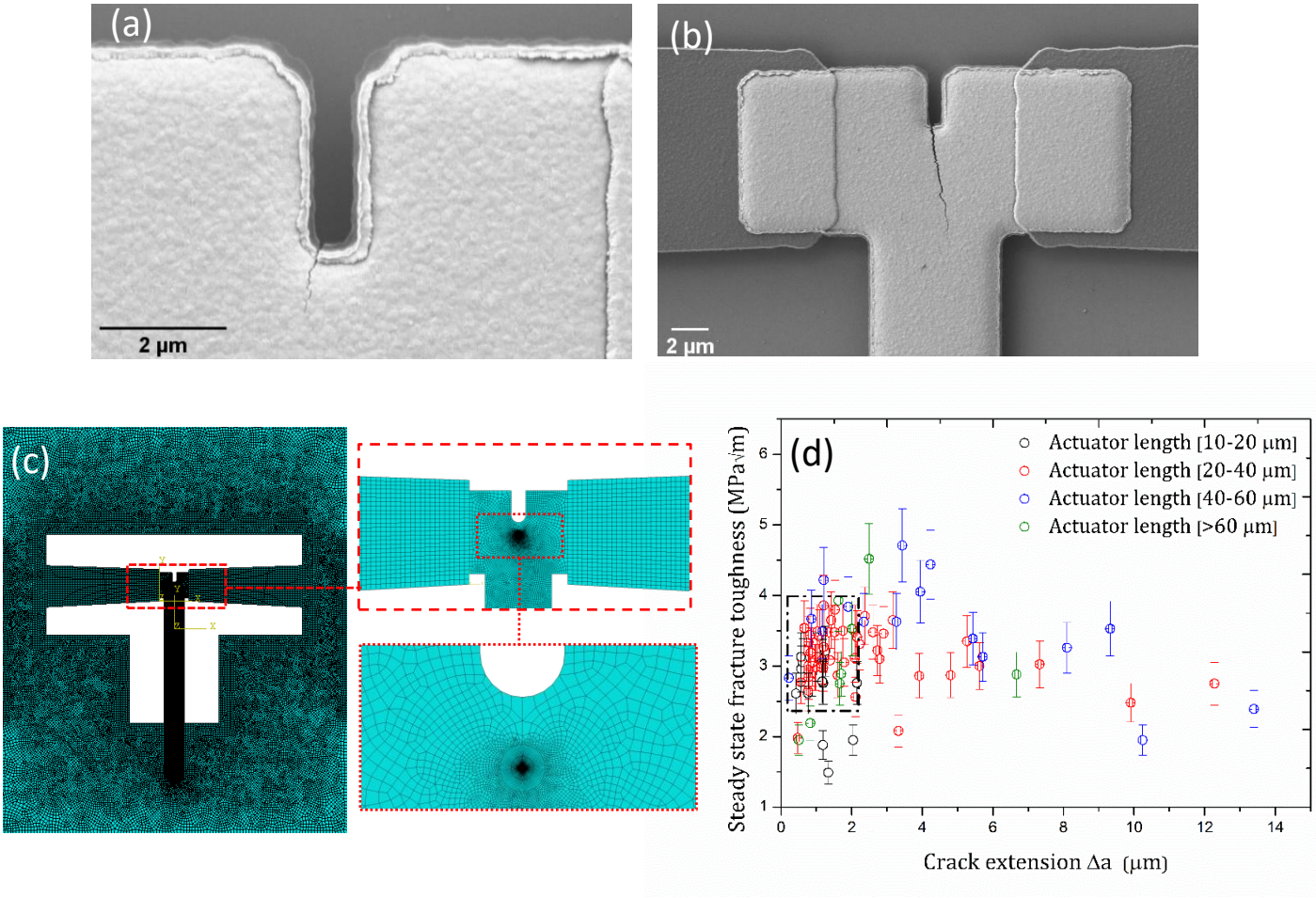

Fig. 4. SEM surface micrographs of some successful crack-on-chip test structures after the release of internal stresses in the actuator, resulting in stable arrested cracks in the tungsten films with extensions of (a) ~ 1.2 µm, for an actuator length of ~ 16.3 µm, and (b) ~ 5.3 µm for an actuator length of ~ 32.1 µm. (d) Steady-state fracture toughness as a function of crack extension, estimated using (c) the 2D plane stress elastic finite element model with the J-integral method applied to a crack of the same length as the one measured experimentally.

Figures (main text)

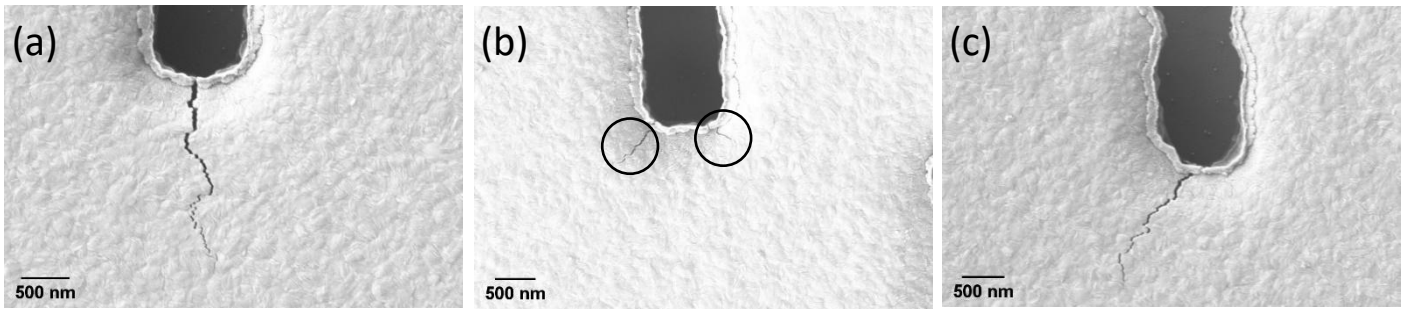

Fig. 5. Selected SEM micrographs of COC test structures illustrating different crack propagation behaviors leading to scatter in fracture toughness values: (a) crack deviation due to the "microstructure effect", (b) initiation and propagation of two cracks due to the "stress state at the notch front effect", (c) side crack propagation due to the "misalignment and notch effect".

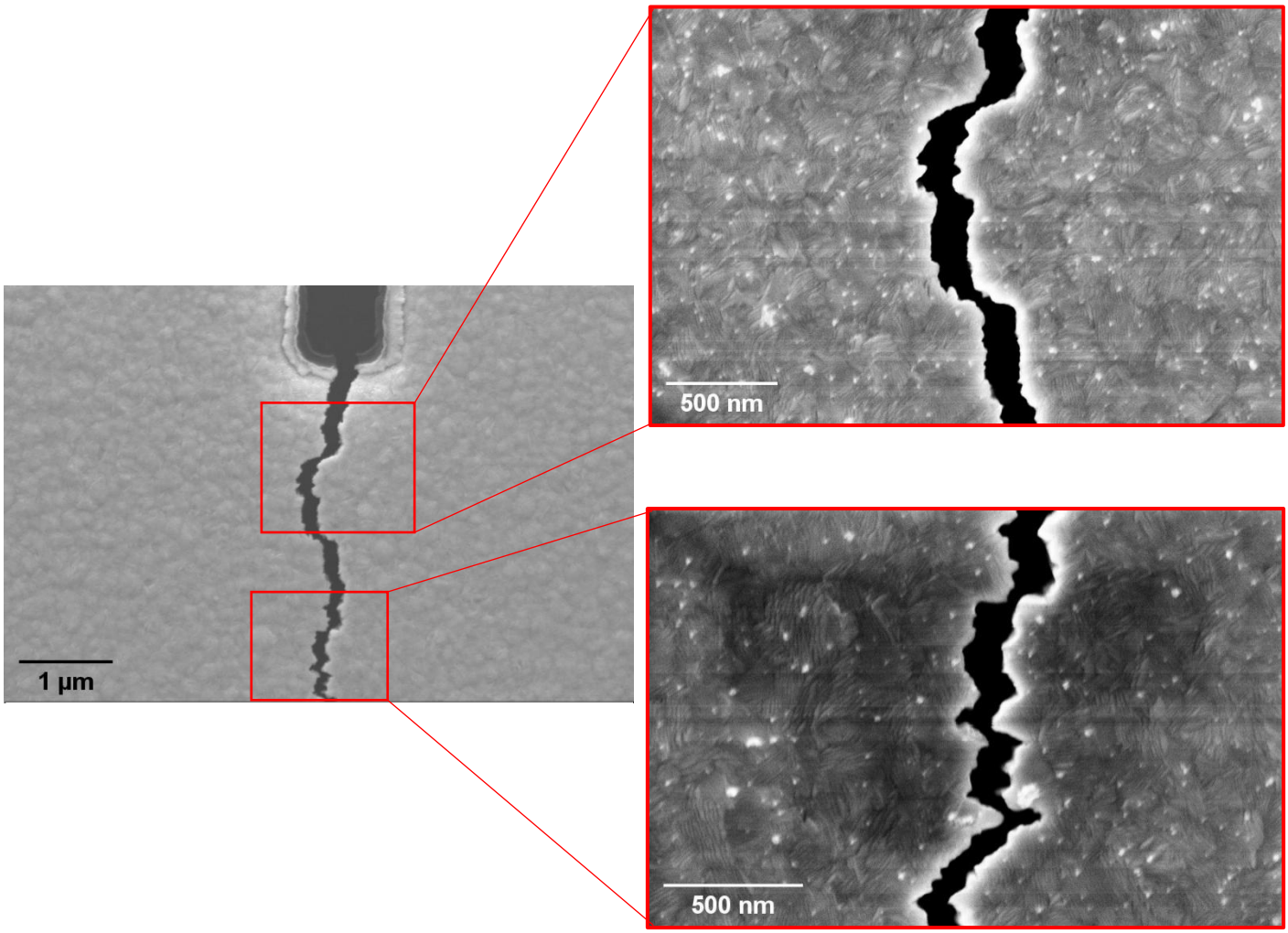

Fig. 6. SEM micrograph of a COC test structure displaying a propagating crack on the left. Zoomed-in images on the right highlight the crack's lips, revealing a smooth morphology with a distorted shape. suggesting local plasticity accompanying the cracking process.

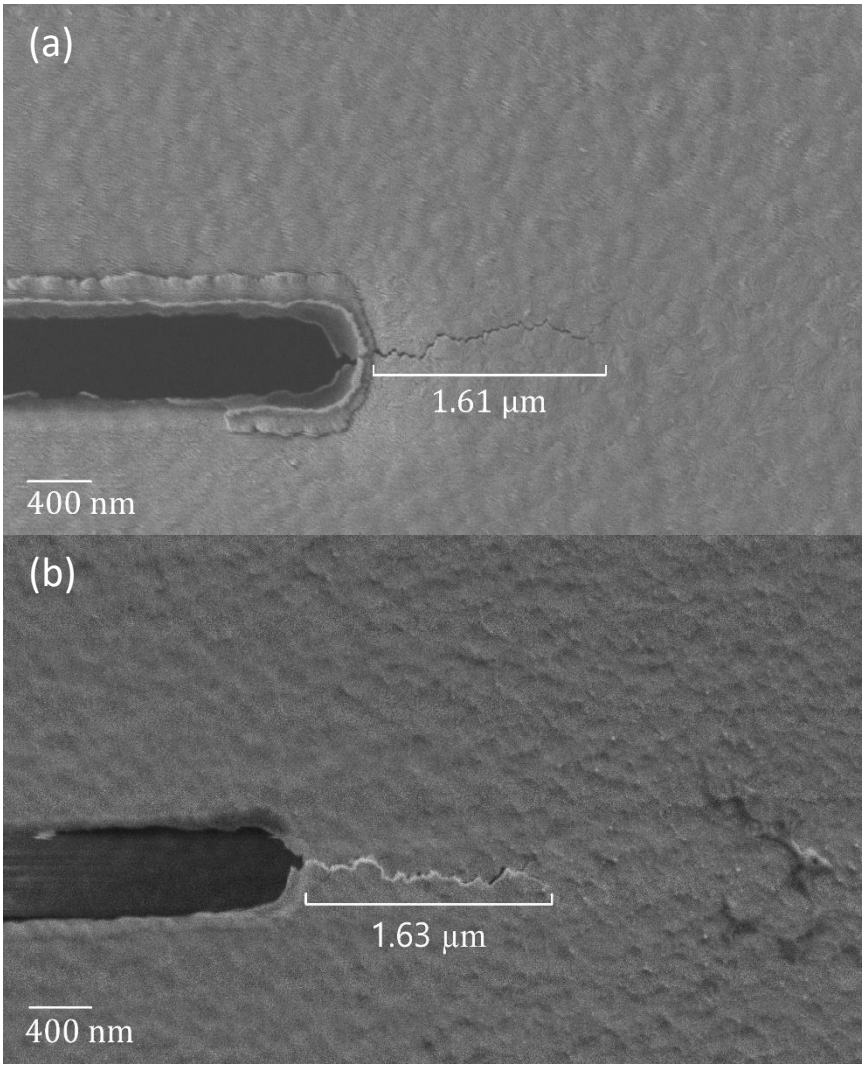

Fig. 7. Focused Ion Beam (FIB) cut W-COC test structure showing crack length comparison between (a) the top surface with a crack length of 1.61 µm and (b) the bottom surface with a crack length of 1.63 µm.

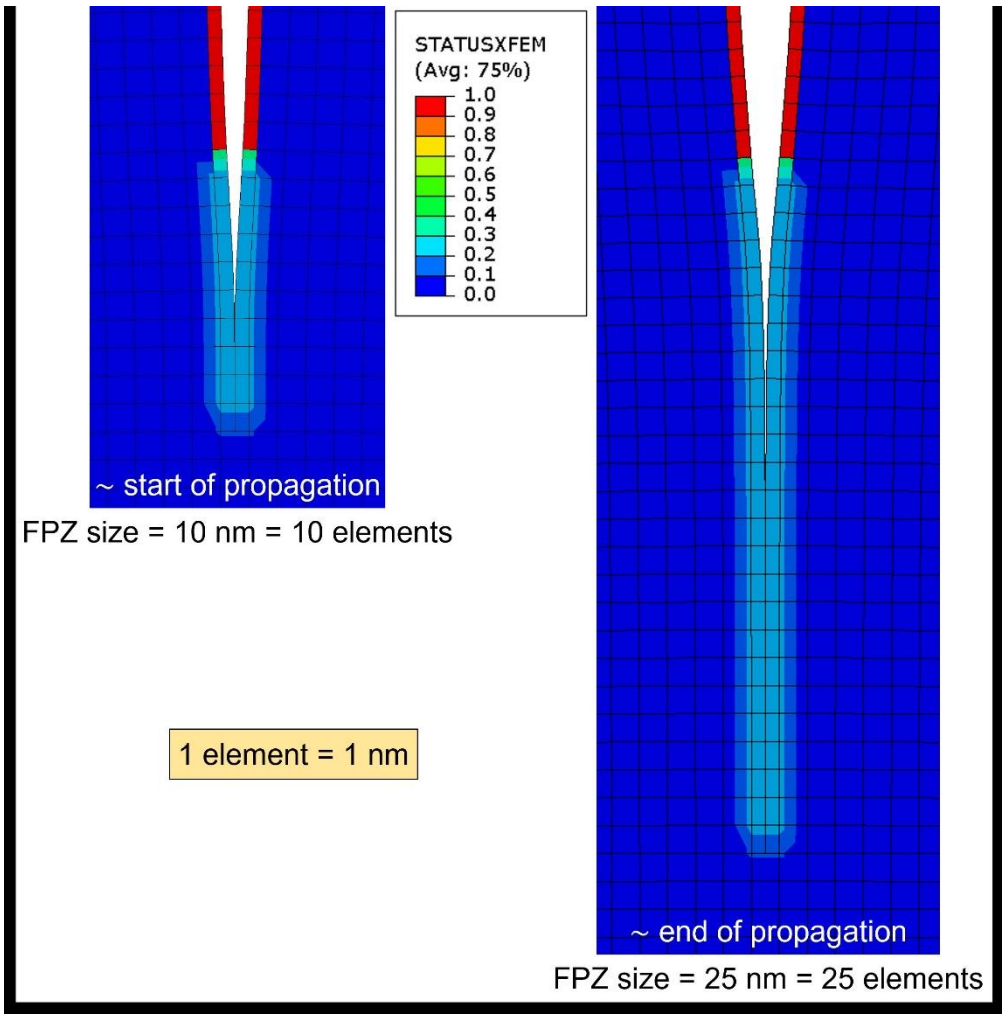

Fig. 8. Snapshot of the near crack tip regions in a cohesive zone-based FE simulation performed with peak strength $\hat{\sigma}$ = 7.8 GPa, cohesive energy $\Gamma_0 \approx 26\ \mathrm{J/m^2}$ and 1nm element size. The left figure corresponds to the situation just after crack initiation, indicating that the FPZ length is around 10 nm. The right figure is when crack arrest is attained, showing that the FPZ length is around 25 nm. This indicates that element sizes on the order of 1 nm are needed to resolve the extremely small FPZ associated with the brittle failure mechanism under investigation.

Figures (main text)

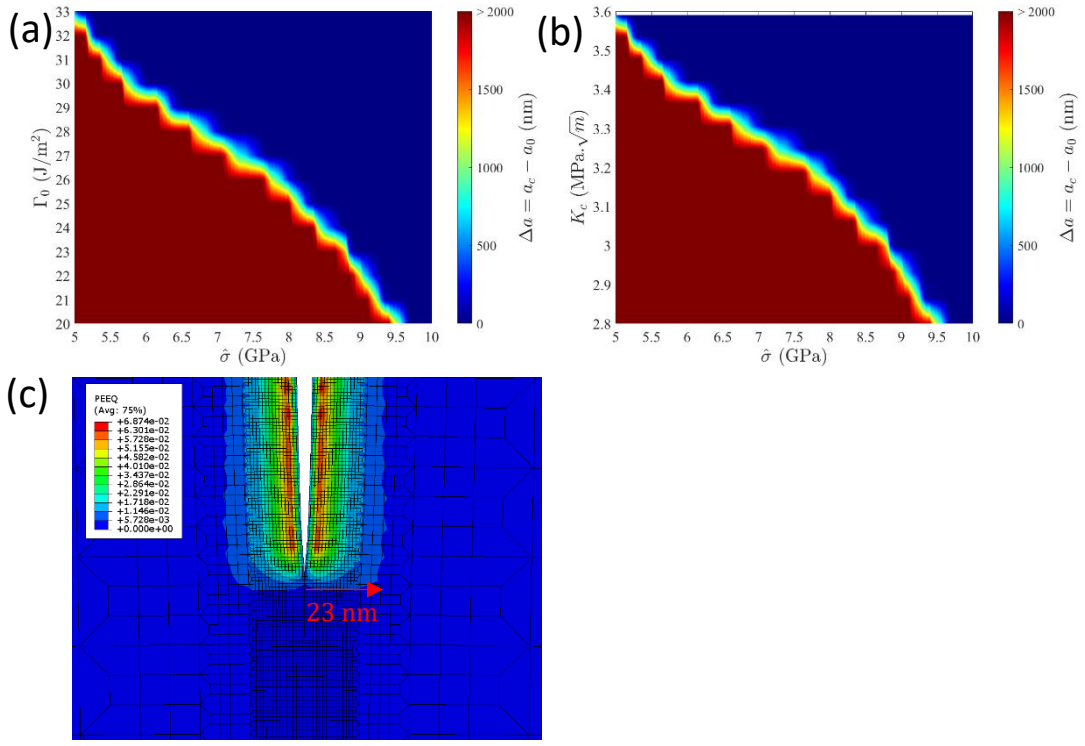

Fig. 9. (a) Map of the measured crack extensions Δa in the space of the imposed $\hat{\sigma} - \Gamma_0$, obtained with the 2D plane strain elastic-plastic XFEM model. (b) Same map, with the fracture energy values Γ_0 analytically converted to fracture toughness values K_{Ic}, assuming no R-effect and using the plane strain assumption. (c) Equivalent plastic strain at the crack tip (with a crack extension of 1 µm) in its crack arrest configuration after the release of internal stresses in the actuator for a parameter set of $\hat{\sigma}$ = 7.8 GPa and Γ_0 = 26 J/m² ($K_{Ic} \approx$ 3.2 MPa√m).